ACS APPLIED MATERIALS & INTERFACES

www.acsami.org

Research Article

Composition-Tunable Bandgap Engineering of Horizontally Guided CdS_xSe_{1-x} Nanowalls for High-Performance Photodetectors

Zitong Xu, Qihang Lv, Xuyang Li, You Meng, Johnny C. Ho,* and Pengfei Guo*

Cite This: *ACS Appl. Mater. Interfaces* 2025, 17, 1962−1970

Read Online

ACCESS | Metrics & More | Article Recommendations | Supporting Information

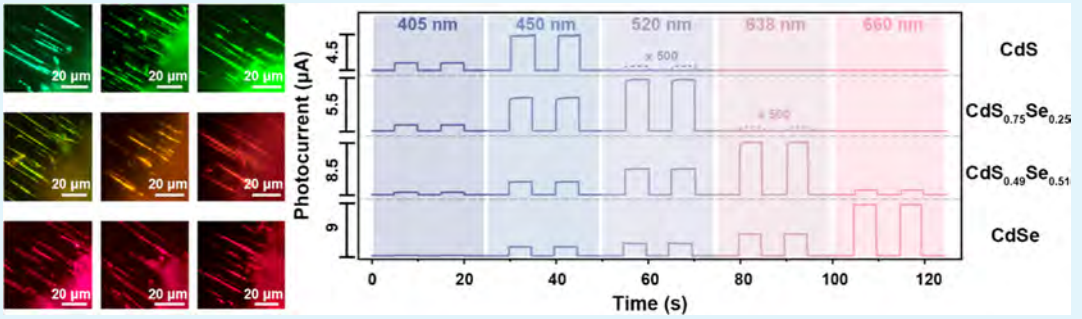

ABSTRACT: Composition-adjustable semiconductor nanomaterials have garnered significant attention due to their controllable bandgaps and electronic structures, providing alternative opportunities to regulate photoelectric properties and develop the corresponding multifunction optoelectronic devices. Nevertheless, the large-scale integration of semiconductor nanomaterials into practical devices remains challenging. Here, we report a synthesis strategy for the well-aligned horizontal CdS_xSe_{1-x} (x = 0−1) nanowall arrays, which are guided grown on an annealed M-plane sapphire using chemical vapor deposition (CVD) approaches. Microstructural characterizations demonstrate these structures as horizontally guided nanowalls with high-quality crystallinity. Microphotoluminescence (μ-PL) reveals the CdS_xSe_{1-x} nanowalls exhibiting continuously tunable spontaneous emissions from 509 nm (pure CdS) to 713 nm (pure CdSe), further confirming that CdS_xSe_{1-x} alloys have a continuously tunable bandgap. Notably, a photodetector based on CdS_xSe_{1-x} nanowalls displays excellent photoelectric performance, such as high responsivity ($3 \times 10^2 \sim 1 \times 10^3$ A/W), high external quantum efficiency ($1.01 \times 10^3 \sim 2.93 \times 10^3$), and fast response speed in the millisecond magnitude. Furthermore, the CdS nanowall-based photodetectors exhibit a remarkable image-sensing capability, indicating potential applications in high-performance image sensing in the future. Bandgap continuously tunable nanowall arrays with high-quality crystallinity inject great vitality into the manufacturing of high-performance integrated optoelectronic devices.

KEYWORDS: *nanowalls, bandgap modulation, graphoepitaxy, guided growth, high-performance photodetector, optoelectronics*

INTRODUCTION

One-dimensional semiconductor nanomaterials provide an excellent material platform for the new generation of optoelectronic devices due to their excellent physical and photoelectric properties.[1−5] In particular, II−VI group semiconductor materials have gained great research interest in the past few years owing to their fascinating properties and unique advantages, such as tunable bandgap, high sensitivity, and excellent photoelectric properties.[6−11] For example, CdS_xSe_{1-x} can achieve tunable optical and electronic properties through composition control, and this flexibility has advantages for photodetectors. In addition, bandgaps of semiconductors are crucial for electronic and optoelectronic applications, and a wide range of continuously tunable bandgaps makes it possible for optoelectronic devices with multispectral response,[12−16] providing great flexibility in the design of high integrated optoelectronic devices[9,17−19] and wavelength-tunable optoelectronic circuits.[20−22]

Bandgap engineering of alloyed semiconductors profoundly impacts the design and development of multifunctional optoelectronic devices.[5,8,20,23−26] For example, the multicomponent-alloyed CdS_xSe_{1-x} nanowires or nanoribbons could be used to construct photodetectors and wavelength-tunable lasers.[22,27,28] GaAsSb and $InAs_xP_{1-x}$ nanowires were applied to multispectral photodetectors.[29,30] $In_xGa_{1-x}N$ nanowires exhibit tunable emissions of 325−850 nm, which can be used in solid-state lighting and solar energy conversion.[31] All-inorganic halide $CsPbX_3$ perovskite nanowires or nanoplatelets were used in tunable nanolasers over a broad visible

Received: October 6, 2024
Revised: November 23, 2024
Accepted: December 11, 2024
Published: December 17, 2024

https://doi.org/10.1021/acsami.4c17135
ACS Appl. Mater. Interfaces 2025, 17, 1962−1970

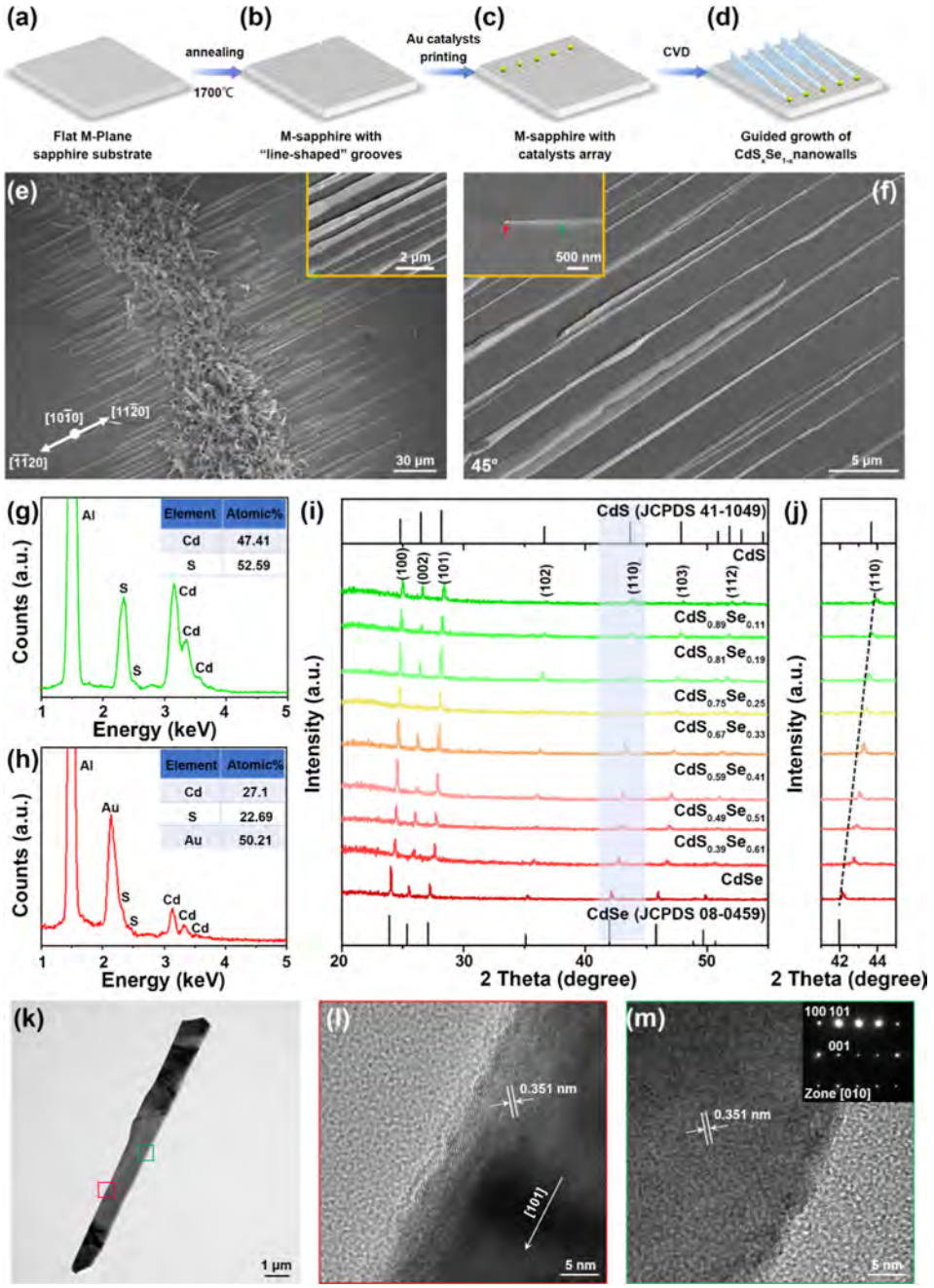

Figure 1. Structural characterization of the CdS_xSe_{1-x} nanowalls. (a−d) Schematic drawing of the experimental process. (e) Low-resolution top-view SEM image and high-resolution SEM image (inset) of the CdS nanowalls grown on annealed M-sapphire. (f) Side-view (the shooting angle is 45°) SEM image of the CdS nanowalls. Inset: SEM image of a typical CdS nanowall. (g,h) EDX spectra of a typical CdS nanowall at the body (green line) and tip (red line) positions, respectively. (i) XRD patterns of the CdS_xSe_{1-x} nanowalls with different compositions. (j) Corresponding enlarged XRD patterns ranging from 41 to 45°. (k) Low-resolution TEM image of a typical CdS nanowall. (l,m) HR-TEM images of two typical positions on the nanowall as indicated in (k). Inset: the corresponding SAED pattern from the nanowall.

range.[19,32,33] Although bandgap-modulated semiconductor nanostructures and devices have made significant progress, constructing optoelectronic devices based on large-scale integrated semiconductor nanostructure arrays remains challenging and underexplored.[34,35] Planar nanowire arrays provide a new platform for large-scale integration of multifunctional optoelectronic devices.[36,37] For example, the horizontal GaN nanowires were used to realize field-effect transistors (FETs) and thin-film transistors,[37] $CsPbBr_3$ planar nanowire arrays were reported for large-area nanowire laser arrays and photodetectors with fast response time,[38−40] the aligned CdS nanowalls were used for high-performance photodetectors and trigate FETs,[41] surface-guided ZnSe@ZnTe core−shell nanowires were utilized to explore its photoelectric properties and exhibit photovoltaic behavior,[42] and the guided growth of $CsPbCl_3/CsPbI_3$ nanowire superlattices was applied to construct photodetectors with higher detection performance and with good image sensing capabilities.[43] All of these unique structures exhibit potential applications for integrated photonics and optoelectronic devices. However, synthesizing horizontally guided nanowalls and arrays remains a significant challenge. To the best of our

https://doi.org/10.1021/acsami.4c17135
ACS Appl. Mater. Interfaces 2025, 17, 1962−1970

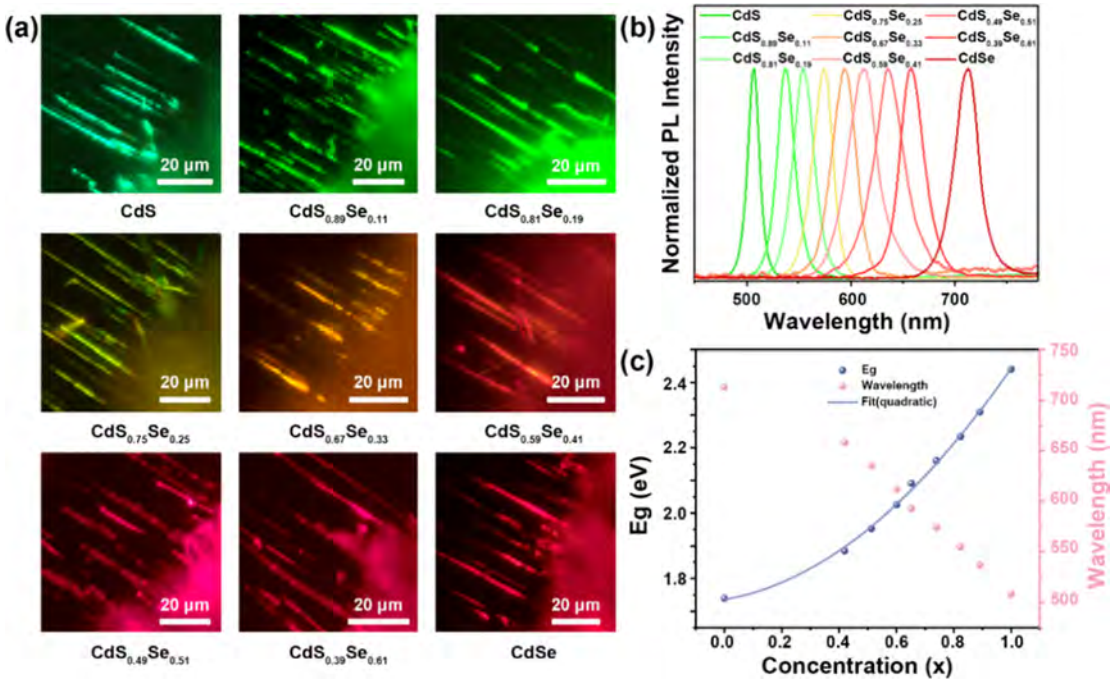

Figure 2. Optical characterization of the CdS_xSe_{1-x} nanowalls. (a) Real-color images of the CdS_xSe_{1-x} alloy nanowalls with various compositions and (b) corresponding PL spectra. (c) Emission wavelength and bandgap of the CdS_xSe_{1-x} nanowalls as a function of alloy composition. Blue spheres represent the bandgaps of the CdS_xSe_{1-x} nanowalls, and pink spheres represent the wavelength of the emission peaks. The blue line is the fitting curve of composition and bandgap.

knowledge, the guided growth of horizontal and aligned CdS_xSe_{1-x} nanowall arrays and corresponding photodetectors have not been reported.

In this work, we report the successful synthesis of surface-guided growth of CdS_xSe_{1-x} nanowalls by the CVD method. The composition of the CdS_xSe_{1-x} nanowalls is adjustable from $x = 0$ to $x = 1$. Structural characterizations, including scanning electron microscopy (SEM) images, energy-dispersive X-ray spectroscopy (EDX), X-ray diffraction (XRD), and transmission electron microscopy (TEM), reveal that these nanowalls have high-quality crystalline with wurtzite structures. The microphotoluminescence (μ-PL) spectra indicate that the PL emission peaks of CdS_xSe_{1-x} structures can be continuously modulated from 509 to 713 nm. Moreover, the photoelectric properties of CdS_xSe_{1-x} nanowall-based photodetectors were systematically investigated, which exhibited a gradually expanded response range, high responsivity, and fast response time. In addition, these nanowalls show the potential in high-resolution imaging applications. These results endow CdS_xSe_{1-x} nanowalls with widespread prospects for developing highly integrated detectors and image sensors.

RESULTS AND DISCUSSION

These guided CdS_xSe_{1-x} nanowall arrays are synthesized via a CVD method, as shown in Figure S1 (see the Supporting Information) and the Experimental Section. First, the M-plane sapphire forms periodic "line-shaped" grooves on the surface owing to thermodynamic instability by annealing at 1700 °C for 10 h, which is used for the guided growth of nanowalls (Figure 1a,b).[37,44] Second, gold nanoparticles are deposited onto the annealed M-plane sapphire as catalysts for growing CdS_xSe_{1-x} nanowall arrays (Figure 1c). Third, the CdS and CdSe powders serve as the source materials, and CdS_xSe_{1-x} nanowall arrays are grown through a CVD method (Figure 1d). Figure 1e shows the low-resolution SEM image of CdS nanowall arrays grown on an annealed M-plane sapphire surface. CdS nanowalls are arranged on the annealed M $(10\bar{1}0)$ sapphire with periodic "line-shaped" grooves along the direction of $\pm 11\bar{2}0$ (Al_2O_3) (Figure S2, see the Supporting Information).[41,45] The length of the nanowalls is about 50−100 μm. After a few seconds of weak ultrasound wash in isopropyl alcohol, the vertically grown nanoribbons can be removed, while the horizontally grown nanowalls remain unchanged (Figure S3; see the Supporting Information). In addition, the morphology of CdS_xSe_{1-x} nanowalls is similar to that of pure CdS nanowalls in Figure S4 (see the Supporting Information), which provides strong evidence for achieving the composition continuously tunable CdS_xSe_{1-x} nanowalls. The side-view SEM image (Figure 1f) shows that the nanowalls are jagged and have a large aspect ratio (height divided by width). The width of the nanowalls is ∼200 nm, and the height is about 1 μm (Figure S5; see the Supporting Information). A typical CdS nanowall shows a gradual decrease in height, and gold nanoparticles can be observed at the tip of the nanowall (inset in Figure 1f), which indicates the vapor−liquid−solid (V−L−S) and vapor−solid (V−S) grown mechanism along the length of the nanowalls.[46] Figure 1g,h exhibits the EDX spectra at the body and tip of a typical CdS nanowall. As can be seen, the body of the nanowall is composed of Cd and S, with an atomic ratio of about 1:1, and the nanosphere catalyst at the tip is constituted of gold, which further indicates the existence of the V−L−S growth mechanism in the growth of nanowalls. As shown in Figure S6 (see the Supporting Information), EDX elemental mapping of Cd and S elements demonstrates a uniform elemental distribution in the CdS nanowall vertical direction. Figure 1i reveals the XRD patterns of these CdS_xSe_{1-x} $(x = 0-1)$ nanowalls. The sharp diffraction peaks of CdS_xSe_{1-x} nanowalls indicate the high crystallinity

https://doi.org/10.1021/acsami.4c17135
ACS Appl. Mater. Interfaces 2025, 17, 1962−1970

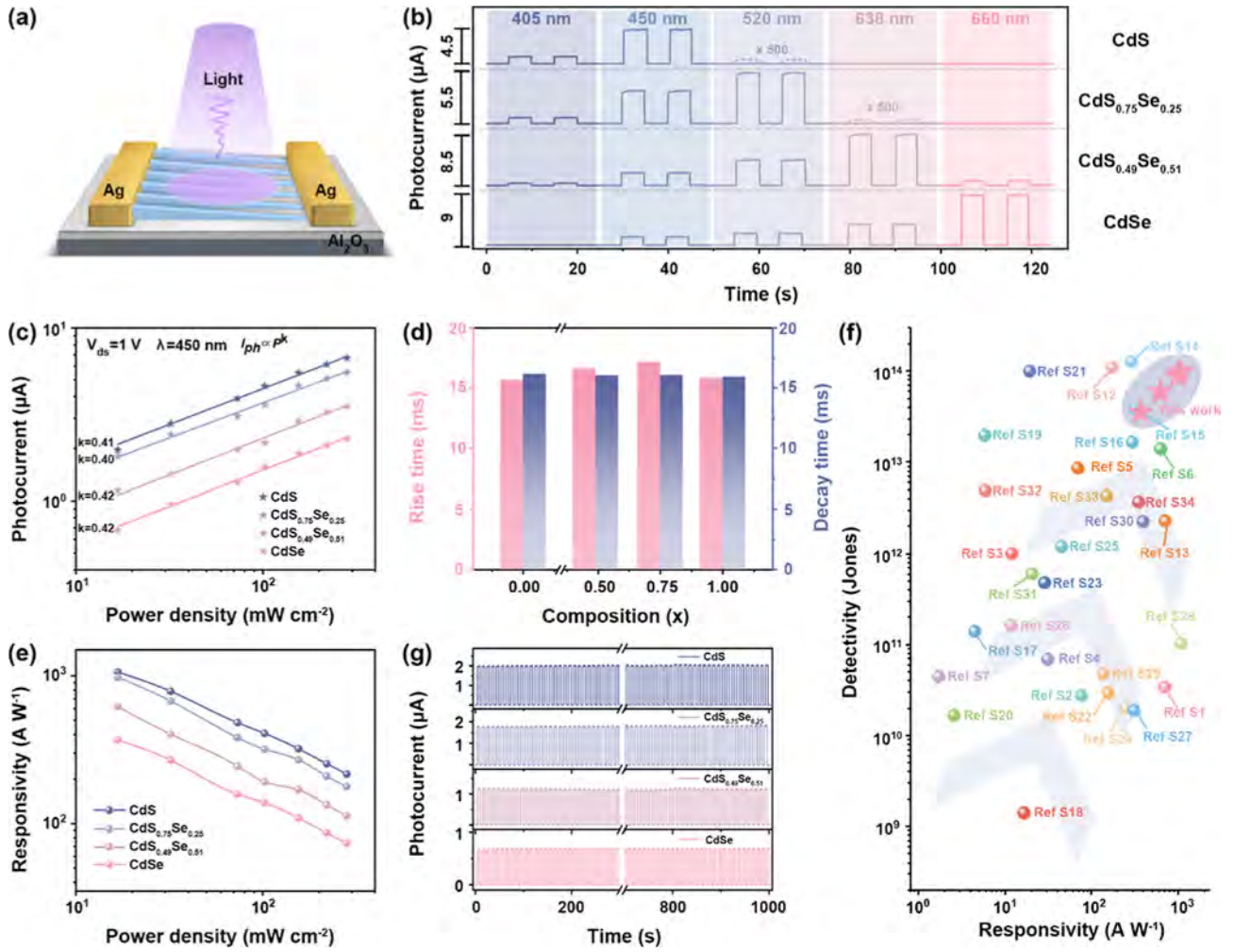

Figure 3. Photoelectric performance based on the CdS_xSe_{1-x} nanowall photodetectors. (a) Schematic diagram of the nanowall photodetector. (b) Photoresponse of CdS_xSe_{1-x} photodetectors under different wavelengths of light illumination at 405, 450, 520, 638, and 660 nm. (c) Relationship between the photocurrent (I_{ph}) and the light power density of CdS_xSe_{1-x} photodetectors under a 450 nm laser illumination. (d) Histogram of the rise time (red) and decay time (blue) of the photodetectors under a 450 nm laser illumination as a function of Se composition. (e) Responsivity of the CdS_xSe_{1-x} photodetectors as a function of the light power density (1 V bias, 450 nm). (f) Comparison of R and D^* of four typical CdS_xSe_{1-x} (x = 0, 0.49, 0.75, and 1) photodetectors. Detailed performance parameters are shown in Table 1. (g) $I-T$ curve of CdS_xSe_{1-x} photodetectors at 1 V bias under a 450 nm laser illumination for 1000 s.

with a hexagonal wurtzite structure, which shows good agreement with hexagonal wurtzite CdS (JCPDS 41-1049) and CdSe (JCPDS 08-0459) standard card, respectively. Figure 1j suggests the amplified XRD pattern from 41 to 45° in Figure 1i, which exhibits the diffraction peak slightly shifting toward a lower angle at the (110) plane, indicating that the lattice expansion is due to the larger atom radius of Se.

Transmission electron microscopy (TEM) was used to investigate the microstructure of these nanowalls by a tungsten-tipped probe and a homemade fiber probe to transfer a representative nanowall on the copper grid, as shown in Figure S7 (see the Supporting Information). Figure 1k is a typical low-resolution TEM image of the selected nanowall. The high-resolution TEM (HR-TEM) images at two typical positions from the nanowall (red and green squares as indicated in Figure 1k) are shown in Figure 1l,m, respectively, where a high-quality single-crystalline nanostructure without significant defects is clearly observed with the lattice spacing of ~0.351 nm, corresponding to the (002) lattice spacing of wurtzite CdS.[8] The inset of Figure 1m shows the corresponding selection region electron diffraction (SAED) pattern, indexing for the [010] crystal zone axis, indicating a high-quality single-crystalline wurtzite structure growing along the [101] direction without obvious defects and dislocations.

The optical properties of the samples were investigated by a confocal optical system, as schematically shown in Figure S8 (Supporting Information). Figure 2a illustrates the real-color images of nine typical CdS_xSe_{1-x} alloy nanowalls with different compositions with x = 0−1 under a 405 nm laser illumination. The emission colors were continuously tuned from green, yellow, and orange to red from nine samples. Figure 2b shows the room-temperature PL spectra of the CdS_xSe_{1-x} samples, which present a continuously tuned PL peaks ranging from 509 to 713 nm with full width at half-maximum (fwhm) of about 20−30 nm. These PL emission spectra with single-shape peaks suggest that the alloy CdS_xSe_{1-x} nanowalls have good crystallinity, which may have potential applications for tunable optoelectronic devices. It can be seen that CdS_xSe_{1-x} nanowalls are composed of Cd, S, and Se with different ratios of S and Se according to the EDX spectra in Figure S9 (see the

https://doi.org/10.1021/acsami.4c17135
ACS Appl. Mater. Interfaces 2025, 17, 1962−1970

Table 1. Comparison of Photoconductivity Performance Based on Semiconductor Nanostructures

materials	R (A/W)	D^* (Jones)	EQE (%)	rise time	decay time	refs
CdS_xSe_{1-x}	1062	9.85×10^{13}	2.93×10^3	15.84 ms	15.94 ms	this work
	979	8.87×10^{13}	2.70×10^3	17.19 ms	16.09 ms	
	621	5.87×10^{13}	1.71×10^3	16.66 ms	16.05 ms	
	368	3.55×10^{13}	1.01×10^3	15.66 ms	16.17 ms	
CdS/CdS_xSe_{1-x}	118		3.1×10^4	~68 μs	~137 μs	S1
CdS	50−171		154−525	<300 ns	<400 ns	S2
CdSSe NWs	670	—	2×10^5	19.6 ms	76.4 ms	S3
CdS_xSe_{1-x}	703	3.41×10^{10}	1.94×10^3	39 ms	39 ms	S4
CdSe NTs	76	2.75×10^{10}		1.85 s	0.20 s	S5
CdSe film	12	1×10^{12}		0.4 ns	~0.25 μm	S6
CdSe nanocrystalline	9.1−31	6.9×10^{10}		<2 μs	<2 μs	S7
CdSe NB	69.11	8.6×10^{12}	1.1×10^4	0.81 ms	0.77 ms	S8
CdS NFAs	629	1.4×10^{13}		150 ms	290 ms	S9
CdSe NW	1.7	4.46×10^{10}		7.5 μs	11 μs	S10
CdSe NW	40			2.4 μs	2.0 μs	S11
$Cs_3Sb_2Br_9$ NF/CdSe NB	174	1.1×10^{14}	4.8×10^4	16.5 ms	15.7 ms	S12
Au NIS@CdSSe NBs	711.4	2.29×10^{12}	1.61×10^5	22.6 ms	23.0 ms	S13
$CsPbBr_3$ NCs/2D CdS_xSe_{1-x}	289	1.28×10^{14}		0.53 s	0.62 s	S14
$CdS@CsPbBr_3$	319.79	3.84×10^{13}		10.1 ms	14.5 ms	S15
ZnS/InP nanowires	295	1.65×10^{13}	1.10×10^{13}	0.75 s	0.5 s	S16
ZnSe	4.44	1.4×10^{11}		0.16 ms	0.13 ms	S17
ZnS NTs	16.5	1.41×10^9		0.12 s	0.4 s	S18
ZnS QDs	5.8	1.97×10^{13}		—	—	S19
ZnS NTs	2.56	1.67×10^{10}		0.09 s	0.07 s	S20
GaS NSs	19.2	10^{14}	9.371×10^3	<2 ms	<30 ms	S21
SnS NFAs	156	2.94×10^{10}	4.77×10^4	5.1 ms	8.8 ms	S22
InAsSb	28.57	4.81×10^{11}		1.8 s	2.4 s	S23
$InP/InAs_{0.4}P_{0.6}$	250	2×10^{10}		33 μs	207 μs	S24
$GaAs_{0.94}Sb_{0.06}$	44.9	1.2×10^{12}	7.1×10^3			S25
1D GaAsSb/2D MoS_2	11.7	1.64×10^{11}	2.74×10^3	50 μs	54 μs	S26
GaAsSb/AlGaAs	311	1.9×10^{10}	6.1×10^4			S27
In_2Se_3	1081.5	1.03×10^{11}	1.92×10^4	8 ms	10 ms	S28
In_2S_3	137	4.74×10^{10}	3.78×10^4	6 ms	8 ms	S29
α-In_2Se_3	395	2.26×10^{12}	1.63×10^5	18 ms	73 ms	S30
PLD-In_2Se_3	20.5	6.02×10^{11}	4.784×10^3	24.6 ms	57.4 ms	S31
β-In_2Se_3/Si	5.9	4.9×10^{12}	1.376×10^3	<8.3 ms	<8.3 ms	S32
GaSe/WS_2	149	4.3×10^{12}		37 μs	43 μs	S33
GaSe/InSe	350	3.7×10^{12}	9.3	1.85 μs	2.05 μs	S34

Supporting Information). Then, the X-ray photoelectron spectroscopy (XPS) analysis was utilized to reveal the composition and elemental existing states of the CdS_xSe_{1-x} nanowalls, with results presented in Figures S10 (see the Supporting Information). In addition, the bandgaps of the CdS_xSe_{1-x} nanowalls can be obtained by this equation ($E_g = \frac{h\nu}{\lambda}$). Next, the absorption spectra of CdS_xSe_{1-x} nanowalls were recorded using an ultraviolet−visible absorption spectrum. The bandgap is calculated using the Tauc equation, and the calculated results are consistent with those obtained from PL spectra (Figure S11, see the Supporting Information). As shown in Figure 2c, the bandgaps of CdS_xSe_{1-x} nanowalls exhibit a nonlinear relationship with the composition x, and the fitting quadratic function is as follows[47,48]

$$E_g(CdS_xSe_{1-x}) = xE_g(CdS) + (1 - x)E_g(CdSe) - x(1 - x)b \quad (1)$$

The calculated bending coefficient b is 0.55 eV, which agrees with the previous report,[49] confirming the continuously tunable composition of CdS_xSe_{1-x} nanowalls.

As shown in Figure 3, the photoelectric performance of CdS_xSe_{1-x} nanowall-based photodetectors is systematically investigated. Figure 3a shows the schematic diagram of the photodetectors based on nanowall arrays. Figure 3b shows the photoresponse properties of four typical CdS_xSe_{1-x} nanowall photodetectors, which are measured by periodically turning on and off lasers at V_{ds} = 1 V. These results show that all the devices exhibit an excellent spectral response to visible light (405−520 nm). In addition, the spectral response range of CdS_xSe_{1-x} photodetectors is gradually extended with the evolution of the Se composition from 0 to 1. The performance of the CdS_xSe_{1-x} photodetectors with different Se compositions under a 450 nm laser illumination is meticulously analyzed in Figures S12−S15 (see the Supporting Information), while the areas of all devices are approximately the same. As can be seen, the photocurrent increases gradually with increasing light intensity, indicating that more photogenerated charge carriers are generated with the increase in power density. The relationship between the photocurrent (I_{ph}) and the light power density can be expressed by the power law function

https://doi.org/10.1021/acsami.4c17135
ACS Appl. Mater. Interfaces 2025, 17, 1962−1970

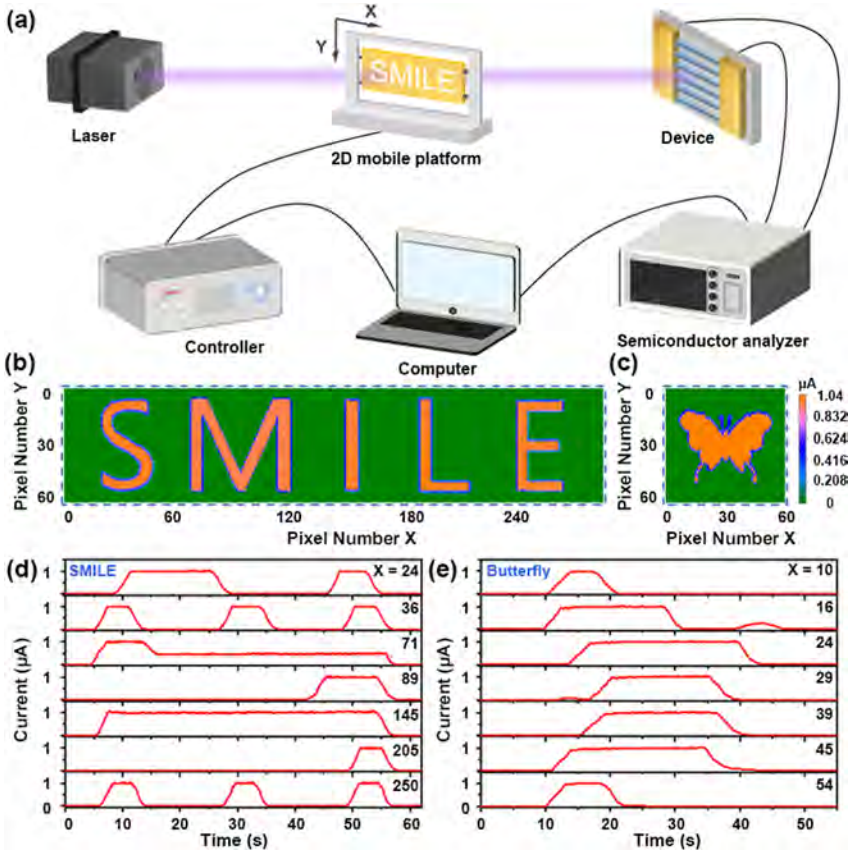

Figure 4. Application of imaging sensor of the CdS nanowall-based photodetectors. (a) Schematic diagram of the imaging system of the CdS nanowall-based photodetectors. (b,c) Imaging results of the "SMILE" and "Butterfly" patterns under a 405 nm laser illumination, respectively. (d,e) Time-resolved current curves of pixel sequences in different X directions when the 405 nm light spot scans the "SMILE" and "Butterfly" masks along the Y direction. The number in the upper right corner indicates the sequence of pixels in the X direction.

$$I_{ph} \propto P^{k} \tag{2}$$

where I_{ph} ($I_{ph} = I_{light} - I_{dark}$) is the photocurrent, P is the light power density, and k is the power exponent. Figure 3c reveals that the extracted k values of CdS_xSe_{1-x} photodetectors with different Se compositions under 450 nm light illumination are calculated as 0.41 (CdS), 0.40 ($CdS_{0.75}Se_{0.25}$), 0.42 ($CdS_{0.49}Se_{0.51}$), and 0.42 (CdSe), respectively. It is worth noting that the sublinear relationship between photocurrent and light power intensity may be caused by defect mechanisms, including recombination centers and traps.[50,51] Subsequently, the photoresponse speed of the photodetector is studied. The response speed can be divided into rise time (τ_r) and decay time (τ_d), defined as the time required for the photocurrent to rise from 10% to 90% of the stable value and to fall from 90% to 10% of the stable value, respectively. Figure 3d shows the comparison of the τ_r and τ_d of CdS_xSe_{1-x} photodetectors with different Se compositions. It can be seen that the CdS_xSe_{1-x} photodetectors exhibit a fast response speed of millisecond magnitude. The response speed of devices elevates with the increasing laser intensity, which has been described by the Rose model.[52,53] The devices have a high I_{ON}/I_{OFF} ratio of 10^5, as shown in Figures S12b–S15b (see the Supporting Information).

Furthermore, in order to further study the photoelectric performance of CdS_xSe_{1-x} photodetectors, some critical parameters of the photodetector are also investigated, such as responsivity (R), specific detectivity (D^*), and external quantum efficiency (EQE), which can be expressed as follows

$$R = \frac{I_{ph}}{PS} \tag{3}$$

$$D^* = R\frac{\sqrt{S}}{\sqrt{2eI_{dark}}} \tag{4}$$

$$\mathrm{EQE} = R\frac{hc}{e\lambda} \tag{5}$$

where S is the effective area under illumination ($S = wdn$, w is the nanowall width, d is the electrode spacing, and n is the number of nanowalls), h is Planck's constant, c is the speed of light in vacuum, λ is the wavelength of the incident light, and e is the electron charge.

The $I_{ds}-V_{ds}$ curves of CdS_xSe_{1-x} photodetectors under dark conditions, as shown in Figure S16 (see the Supporting Information). The responsivity of the CdS_xSe_{1-x} photodetectors with different Se compositions under 450 nm laser illumination versus incident power densities is shown in Figure 3e. With the decrease of Se composition, the R gradually adjusted from 368 A/W ($x = 0$) to 1062 A/W ($x = 1$) under 450 nm laser illumination. Notably, the responsivity decreases with the increased incident power density due to the shorter carrier lifetime and increased carrier recombination under a high incident light.[54,55] Additionally, the variation tendency of EQE and D* are consistent with that of R, which are calculated

https://doi.org/10.1021/acsami.4c17135
ACS Appl. Mater. Interfaces 2025, 17, 1962−1970

to be an EQE of $1.01 \times 10^3 \sim 2.93 \times 10^3$ and a D^* of $3.55 \times 10^{13} \sim 9.85 \times 10^{13}$ Jones, as shown in Figure S17 (see the Supporting Information). To evaluate the performance of these devices, the photoelectric performance of CdS_xSe_{1-x} nanowall-based photodetectors was compared with those reported in the literature (Figure 3f and Table 1). It is worth noting that the CdS_xSe_{1-x} nanowall-based photodetectors show better comprehensive performance. It can be explained from the following aspects: (I) the fabricated CdS_xSe_{1-x} nanowall through a CVD method has a high crystalline quality, with no obvious defect emission and few structural defects. (II) Due to its large specific surface area, the CdS_xSe_{1-x} nanowall can enhance the light absorption area, and the material can absorb more photons compared with other nanostructures. (III) Compared with traditional integrated nanostructures,[56,57] horizontally arranged nanostructures can effectively avoid damage to nanostructures due to additional manufacturing steps. These results indicate the significant tunability of the photoelectric properties through alloy engineering of CdS_xSe_{1-x} nanowalls. Furthermore, stability is another key parameter for the practical application of photodetectors. To investigate the stability of the CdS_xSe_{1-x} photodetectors, the optical response of the devices is measured under a 450 nm laser illumination and 1 V bias for 1000 s. As shown in Figure 3g, the photodetector shows a good cyclic response, and the photocurrent does not change significantly, indicating that the CdS_xSe_{1-x} photodetectors have a repeatable and stable response.

Considering the high photosensitivity of the CdS_xSe_{1-x} nanowall-based photodetectors, the device may have good potential for image-sensing applications. The schematic diagram of the imaging principle is shown in Figure 4a. A 405 nm laser serves as the light source. The image masks with hollow "SMILE" and "Butterfly" patterns are placed between the light source and the detector, assisted by a 2D mobile platform, which can be moved continuously along the horizontal and vertical directions (i.e., the X and Y directions), respectively. During the image-sensing process, the electrical signals of the nanowalls are recorded in real time by a semiconductor analyzer and then converted to the corresponding "SMILE" and "Butterfly" images (Figure 4b,c). The images "SMILE" and "Butterfly" are scanned by a 405 nm laser with pixel sequences in the X direction along the Y direction; the time-resolved current curves of the nanowall-based photodetectors are exhibited in Figure 4d,e, respectively. The patterns are accurately presented with distinct edges and consistent shading, demonstrating the potential of nanowall-based photodetectors for future micro/nano-optoelectronic image sensing applications.

CONCLUSIONS

In summary, using a graphoepitaxy effect, horizontally aligned CdS_xSe_{1-x} nanowall arrays were synthesized on an annealed M-plane sapphire. Structural and optical characterizations reveal that these nanowalls have wurtzite crystal structures, tunable chemical composition ($0 \leq x \leq 1$), and tunable optical bandgaps. On this basis, the photodetectors are constructed based on these unique structures, which exhibit a broadband photodetection with the tunable spectral response, high responsivity ($3 \times 10^2 \sim 1 \times 10^3$ A/W), and fast response speed (rise time ~15.66 ms and decay time ~15.94 ms). In addition, we demonstrate these devices' impressive imaging sensing capabilities in a self-built imaging system. These results indicate that the large-scale production of high-quality CdS_xSe_{1-x} nanowall arrays brings broad prospects for integrated photodetectors and high-resolution imaging sensors.

EXPERIMENTAL SECTION

Nanowall Synthesis. CdS_xSe_{1-x} nanowalls were grown using the CVD strategy in a single-zone tube furnace, as schematically shown in Figure S1 (see the Supporting Information). A tube furnace (OTF-1200X) was used to fabricate the nanowall structures with a 2 in. quartz tube (inner diameter 45 mm and length 180 cm). For example, before the growth of CdS nanowalls, the M-plane sapphire was annealed at 1700 °C for 10 h in a high-temperature furnace (KRX-17B). After annealing, 2 nm Au nanoparticles were prepared by an ion sputtering instrument using mask technology. The alumina boat (74 mm in length) filled with CdS powder (Alfa Aesar, 99.999%, 0.07 g) was placed in the center of the heating zone. Several M-plane sapphires coated with 2 nm-thick Au nanoparticles were placed in the deposition area. Before heating, a N_2 flow was introduced into the system at a rate of 60 sccm for 30 min to purge the air and moisture inside the tube. After that, the N_2 flow was increased to 100 sccm, while the pressure in the tube was maintained at 45 Torr. Then, the furnace was heated to 820 °C at a rate of 26 °C/min, and the growth time was 30 min. After growth, the furnace was naturally cooled to room temperature. The alloyed CdS_xSe_{1-x} nanowall arrays were prepared by a similar growth process, in which different proportions of CdS and CdSe (Alfa Aesar, 99.995%) powders were uniformly mixed and placed in the alumina boat at the heating center. Other growth parameters (such as temperature and pressure) were slightly different, as shown in Figure S1 (Supporting Information).

Materials Characterization. The morphology of CdS_xSe_{1-x} alloy nanowalls was observed by scanning electron microscopy (SEM, Hitachi SU-8010) with energy-dispersive X-ray spectroscopy (EDX). The crystallinity of these alloy nanowalls was studied by X-ray diffraction (XRD, Bruker D8). The crystal structures were determined by transmission electron microscopy (TEM, JEM-F200). The optical images and PL spectra of the nanowalls were tested by using a self-made confocal optical system. A 375 nm laser beam was focused to a spot size of about 0.5 μm employing a microscope lens (Nikon, ×100) and locally excited at the nanowalls. The PL spectra were recorded with an optical spectrometer (Maya Pro2000), and real-color images were recorded with a CCD camera.

Device Fabrication and Characterization. The copper mesh is used as a mask plate to determine the electrode patterns and their gap. The device arrays were fabricated via the direct thermal evaporation of 500 nm Ag particles with the vapor passing through a shadow mask placed on the samples. All device measurements were performed on the probe station with a semiconductor parameter analyzer system (Keithley 2450) in an ambient environment at room temperature. The 405, 450, 520, 638, and 660 nm lasers illuminated the device. The movement of the image pattern mask is controlled by a stepper motor (Zolix-SC300).

ASSOCIATED CONTENT

Supporting Information

The Supporting Information is available free of charge at https://pubs.acs.org/doi/10.1021/acsami.4c17135.

CVD setup, SEM image, EDX spectra, optical photographs, and optical microscope images of the micromanipulation process by the tungsten tipped probe and a homemade fiber probe, schematic diagram of confocal microscopy system, and optoelectronic characterization of the CdS_xSe_{1-x} nanowall (PDF)

AUTHOR INFORMATION

Corresponding Authors

Pengfei Guo − *College of Physics and Optoelectronics, Taiyuan University of Technology, Taiyuan 030024, China;*

https://doi.org/10.1021/acsami.4c17135
ACS Appl. Mater. Interfaces 2025, 17, 1962−1970

orcid.org/0000-0002-4785-0753;
Email: guopengfei2010@126.com

Johnny C. Ho − *Institute for Materials Chemistry and Engineering, Kyushu University, Fukuoka 816 8580, Japan; Department of Materials Science and Engineering, City University of Hong Kong, Kowloon 999077, China;* orcid.org/0000-0003-3000-8794; Email: johnnyho@cityu.edu.hk

Authors

Zitong Xu − *College of Physics and Optoelectronics, Taiyuan University of Technology, Taiyuan 030024, China*

Qihang Lv − *College of Physics and Optoelectronics, Taiyuan University of Technology, Taiyuan 030024, China*

Xuyang Li − *College of Physics and Optoelectronics, Taiyuan University of Technology, Taiyuan 030024, China*

You Meng − *Department of Materials Science and Engineering, City University of Hong Kong, Kowloon 999077, China*

Complete contact information is available at: https://pubs.acs.org/10.1021/acsami.4c17135

Notes

The authors declare no competing financial interest.

■ ACKNOWLEDGMENTS

The authors acknowledge the assistance of the Instrumental Analysis Center at Taiyuan University of Technology. The authors are grateful to the National Natural Science Foundation of China (No. 52373246) and the Fundamental Research Program of Shanxi Provinces (No. 20210302123128) for financial support.

■ REFERENCES

(1) Yang, P. Semiconductor Nanowire, What's Next II? *Next Mater.* **2023**, *1* (2), 100014.

(2) Dasgupta, N. P.; Sun, J.; Liu, C.; Brittman, S.; Andrews, S. C.; Lim, J.; Gao, H.; Yan, R.; Yang, P. 25Th Anniversary Article: Semiconductor Nanowires–Synthesis, Characterization, and Applications. *Adv. Mater.* **2014**, *26* (14), 2137−2184.

(3) Weber, J.; Singhal, R.; Zekri, S.; Kumar, A. One-Dimensional Nanostructures: Fabrication, Characterisation and Applications. *Int. Mater. Rev.* **2008**, *53* (4), 235−255.

(4) Chattopadhyay, S.; Chen, L.; Chen, K. Energy Production and Conversion Applications of One-Dimensional Semiconductor Nanostructures. *NPG Asia Mater.* **2011**, *3* (8), 74−81.

(5) Quan, L. N.; Kang, J.; Ning, C.; Yang, P. Nanowires for Photonics. *Chem. Rev.* **2019**, *119* (15), 9153−9169.

(6) Jie, J.; Zhang, W.; Bello, I.; Lee, C.; Lee, S. One-Dimensional II−VI Nanostructures: Synthesis, Properties and Optoelectronic Applications. *Nano Today* **2010**, *5* (4), 313−336.

(7) Li, L.; Lu, H.; Yang, Z.; Tong, L.; Bando, Y.; Golberg, D. Bandgap-Graded CdS_xSe_{1-X} Nanowires for High-Performance Field-Effect Transistors and Solar Cells. *Adv. Mater.* **2013**, *25* (8), 1109−1113.

(8) Guo, P.; Yang, Q.; Shen, X.; Lv, Q.; Hao, Y.; Xiao, L.; Ho, J. C.; Yu, K. M. Room-Temperature Broad-Wavelength-Tunable Single-Mode Lasing from Alloyed $CdS_{1-x}Se_x$ Nanotripods. *ACS Nano* **2022**, *16* (8), 12767−12776.

(9) Li, H.; Wang, X.; Zhu, X.; Duan, X.; Pan, A. Composition Modulation in One-Dimensional and Two-Dimensional Chalcogenide Semiconductor Nanostructures. *Chem. Soc. Rev.* **2018**, *47* (20), 7504−7521.

(10) Guo, P.; Hu, W.; Zhang, Q.; Zhuang, X.; Zhu, X.; Zhou, H.; Shan, Z.; Xu, J.; Pan, A. Semiconductor Alloy Nanoribbon Lateral Heterostructures for High-Performance Photodetectors. *Adv. Mater.* **2014**, *26* (18), 2844−2849.

(11) Liu, S.; Zhang, L.; Ma, B.; Zeng, X.; Liu, Y.; Ma, Z.; Yang, Z.; Wang, X. *H*igh-Performance Ultraviolet to Near-Infrared Antiambipolar Photodetectors Based on 1D CdS_xSe_{1-x}/2D Te Heterojunction. *ACS Appl. Mater. Interfaces* **2024**, *16*, 47808−47819.

(12) Wang, L.; Yuan, G. D.; Duan, R. F.; Huang, F.; Wei, T. B.; Liu, Z. Q.; Wang, J. X.; Li, J. M. Tunable Bandgap in Hybrid Perovskite $CH_3NH_3Pb(Br_{3-y}X_y)$ Single Crystals and Photodetector Applications. *AIP Adv.* **2016**, *6* (4), 045115.

(13) Guo, P.; Xu, J.; Gong, K.; Shen, X.; Lu, Y.; Qiu, Y.; Xu, J.; Zou, Z.; Wang, C.; Yan, H.; Luo, Y.; Pan, A.; Zhang, H.; Ho, J. C.; Yu, K. M. On-Nanowire Axial Heterojunction Design for High-Performance Photodetectors. *ACS Nano* **2016**, *10* (9), 8474−8481.

(14) Li, W.; Liu, Y.; Huang, X.; Jiang, S.; Zhao, C.; Mai, W. Interfacial Gradient-Energy-Band-Alignment Modulation via a Vapor-Phase Anion-Exchange Reaction toward Lead-Free Perovskite Photodetectors with Excellent UV Imaging Capability. *ACS Appl. Mater. Interfaces* **2021**, *13*, 53194−53201.

(15) Fang, J.; Zhou, Z.; Xiao, M.; Lou, Z.; Wei, Z.; Shen, G. Recent Advances in Low-Dimensional Semiconductor Nanomaterials and their Applications in High-Performance Photodetectors. *InfoMat* **2020**, *2* (2), 291−317.

(16) Jiang, S.; Huang, R.; Li, W.; Huang, X.; Sheng, H.; Wu, F.; Lv, Y.; Fu, Y.; Zhao, C.; Mai, W. Low-Temperature Vapor-Phase Anion-Exchange Strategy for Wide-Bandgap Double-Perovskite Cs_2 $AgBiCl_6$ Films toward Weak Ultraviolet Light Imaging. *ACS Appl. Mater. Interfaces* **2022**, *14*, 26279−26286.

(17) Nichols, P. L.; Liu, Z.; Yin, L.; Turkdogan, S.; Fan, F.; Ning, C. Z. $Cd_xPb_{1-x}S$ Alloy Nanowires and Heterostructures with Simultaneous Emission in Mid-Infrared and Visible Wavelengths. *Nano Lett.* **2015**, *15* (2), 909−916.

(18) Kwon, S. J.; Jeong, H.; Jung, K.; Ko, D.; Ko, H.; Han, I.; Kim, G. T.; Park, J. *S*tructural Origin of the Band Gap Anomaly of Quaternary Alloy $Cd_xZn_{1-x}S_ySe_{1-y}$ Nanowires, Nanobelts, and Nanosheets in the Visible Spectrum. *ACS Nano* **2015**, *9* (5), 5486−5499.

(19) Zhang, Q.; Su, R.; Liu, X.; Xing, J.; Sum, T. C.; Xiong, Q. High-Quality Whispering-Gallery-Mode Lasing from Cesium Lead Halide Perovskite Nanoplatelets. *Adv. Funct. Mater.* **2016**, *26* (34), 6238−6245.

(20) Gao, H.; Feng, J.; Pi, Y.; Zhou, Z.; Zhang, B.; Wu, Y.; Wang, X.; Jiang, X.; Jiang, L. Bandgap Engineering of Single-Crystalline Perovskite Arrays for High-Performance Photodetectors. *Adv. Funct. Mater.* **2018**, *28* (46), 1804349.

(21) Fan, P.; Liu, H.; Zhuang, X.; Zheng, W.; Ge, C.; Huang, W.; Yang, X.; Liu, Y.; Jiang, Y.; Zhu, X.; Pan, A. Ultra-Long Distance Carrier Transportation in Bandgap-Graded CdS_xSe_{1-x} Nanowire Waveguides. *Nanoscale* **2019**, *11* (17), 8494−8501.

(22) Dai, J.; Zhou, P.; Lu, J.; Zheng, H.; Guo, J.; Wang, F.; Gu, N.; Xu, C. The Excitonic Photoluminescence Mechanism and Lasing Action in Band-Gap-Tunable $CdS_{1-x}Se_x$ nanostructures. *Nanoscale* **2016**, *8* (2), 804−811.

(23) Ning, C.; Dou, L.; Yang, P. Bandgap Engineering in Semiconductor Alloy Nanomaterials with Widely Tunable Compositions. *Nat. Rev. Mater.* **2017**, *2* (12), 17070.

(24) Yang, Z. Y.; Albrow-Owen, T.; Cui, H. X.; Alexander-Webber, J.; Gu, F. X.; Wang, X. M.; Wu, T. C.; Zhuge, M. H.; Williams, C.; Wang, P.; Zayats, A. V.; Cai, W. W.; Dai, L.; Hofmann, S.; Overend, M.; Tong, L. M.; Yang, Q.; Sun, Z. P.; Hasan, T. Single-nanowire spectrometers. *Science* **2019**, *365* (6457), 1017−1020.

(25) Yang, Z.; Xu, J.; Wang, P.; Zhuang, X.; Pan, A.; Tong, L. On-Nanowire Spatial Band Gap Design for White Light Emission. *Nano Lett.* **2011**, *11* (11), 5085−5089.

(26) Zhuang, X.; Ning, C. Z.; Pan, A. Composition and Bandgap-Graded Semiconductor Alloy Nanowires. *Adv. Mater.* **2012**, *24* (1), 13−33.

(27) Hu, X.; Liu, H.; Wang, X.; Zhang, X.; Shan, Z.; Zheng, W.; Li, H.; Wang, X.; Zhu, X.; Jiang, Y.; Zhang, Q.; Zhuang, X.; Pan, A. Wavelength Selective Photodetectors Integrated On a Single

Composition-Graded Semiconductor Nanowire. *Adv. Opt. Mater.* **2018**, *6* (12), 1800293.
(28) Pan, J.; Utama, M. I. B.; Zhang, Q.; Liu, X.; Peng, B.; Wong, L. M.; Sum, T. C.; Wang, S.; Xiong, Q. Composition-Tunable Vertically Aligned CdS_xSe_{1-x} Nanowire Arrays Via Van Der Waals Epitaxy: Investigation of Optical Properties and Photocatalytic Behavior. *Adv. Mater.* **2012**, *24* (30), 4151−4156.
(29) Li, Z.; Trendafilov, S.; Zhang, F.; Allen, M. S.; Allen, J. W.; Dev, S. U.; Pan, W.; Yu, Y.; Gao, Q.; Yuan, X.; Yang, I.; Zhu, Y.; Bhat, A.; Peng, S. X.; Lei, W.; Tan, H. H.; Jagadish, C.; Fu, L. Broadband GaAsSb Nanowire Array Photodetectors for Filter-Free Multispectral Imaging. *Nano Lett.* **2021**, *21* (17), 7388−7395.
(30) Ren, P.; Hu, W.; Zhang, Q.; Zhu, X.; Zhuang, X.; Ma, L.; Fan, X.; Zhou, H.; Liao, L.; Duan, X.; Pan, A. Band-Selective Infrared Photodetectors with Complete-Composition-Range $InAs_xP_{1-x}$ Alloy Nanowires. *Adv. Mater.* **2014**, *26* (44), 7444−7449.
(31) Kuykendall, T.; Ulrich, P.; Aloni, S.; Yang, P. Complete Composition Tunability of InGaN Nanowires Using a Combinatorial Approach. *Nat. Mater.* **2007**, *6* (12), 951−956.
(32) Fu, Y.; Zhu, H.; Stoumpos, C. C.; Ding, Q.; Wang, J.; Kanatzidis, M. G.; Zhu, X.; Jin, S. Broad Wavelength Tunable Robust Lasing From Single-Crystal Nanowires of Cesium Lead Halide Perovskites ($CsPbX_3$, X = Cl, Br, I). *ACS Nano* **2016**, *10* (8), 7963−7972.
(33) Park, K.; Lee, J. W.; Kim, J. D.; Han, N. S.; Jang, D. M.; Jeong, S.; Park, J.; Song, J. K. Light-Matter Interactions in Cesium Lead Halide Perovskite Nanowire Lasers. *J. Phys. Chem. Lett.* **2016**, *7* (18), 3703−3710.
(34) Nikoobakht, B.; Michaels, C. A.; Stranick, S. J.; Vaudin, M. D. Horizontal Growth and in Situ Assembly of Oriented Zinc Oxide Nanowires. *Appl. Phys. Lett.* **2004**, *85* (15), 3244−3246.
(35) Wang, X.; Aroonyadet, N.; Zhang, Y.; Mecklenburg, M.; Fang, X.; Chen, H.; Goo, E.; Zhou, C. Aligned Epitaxial SnO_2 Nanowires On Sapphire: Growth and Device Applications. *Nano Lett.* **2014**, *14* (6), 3014−3022.
(36) Rothman, A.; Dubrovskii, V. G.; Joselevich, E. Kinetics and Mechanism of Planar Nanowire Growth. *Proc. Natl. Acad. Sci. U.S.A.* **2020**, *117* (1), 152−160.
(37) Tsivion, D.; Schvartzman, M.; Popovitz-Biro, R.; von Huth, P.; Joselevich, E. Guided Growth of Millimeter-Long Horizontal Nanowires with Controlled Orientations. *Science* **2011**, *333* (6045), 1003−1007.
(38) Fan, C.; Zhu, M.; Xu, X.; Wang, P.; Zhang, Q.; Dai, X.; Yang, K.; He, H.; Ye, Z. Self-Competitive Growth of $CsPbBr_3$ Planar Nanowire Array. *Nano Lett.* **2024**, *24* (12), 3750−3758.
(39) Oksenberg, E.; Sanders, E.; Popovitz-Biro, R.; Houben, L.; Joselevich, E. Surface-Guided $CsPbBr_3$ Perovskite Nanowires On Flat and Faceted Sapphire with Size-Dependent Photoluminescence and Fast Photoconductive Response. *Nano Lett.* **2018**, *18* (1), 424−433.
(40) Wang, X.; Shoaib, M.; Wang, X.; Zhang, X.; He, M.; Luo, Z.; Zheng, W.; Li, H.; Yang, T.; Zhu, X.; Ma, L.; Pan, A. High-Quality in-Plane Aligned $CsPbX_3$ Perovskite Nanowire Lasers with Composition-Dependent Strong Exciton-Photon Coupling. *ACS Nano* **2018**, *12* (6), 6170−6178.
(41) Xu, J.; Oksenberg, E.; Popovitz-Biro, R.; Rechav, K.; Joselevich, E. Bottom-Up Tri-Gate Transistors and Submicrosecond Photodetectors From Guided CdS Nanowalls. *J. Am. Chem. Soc.* **2017**, *139* (44), 15958−15967.
(42) Oksenberg, E.; Martí-Sánchez, S.; Popovitz-Biro, R.; Arbiol, J.; Joselevich, E. Surface-Guided Core-Shell ZnSe@ZnTe Nanowires as Radial P−N Heterojunctions with Photovoltaic Behavior. *ACS Nano* **2017**, *11* (6), 6155−6166.
(43) Lv, Q.; Shen, X.; Li, X.; Meng, Y.; Yu, K. M.; Guo, P.; Xiao, L.; Ho, J. C.; Duan, X.; Duan, X. On-Wire Design of Axial Periodic Halide Perovskite Superlattices for High-Performance Photodetection. *ACS Nano* **2024**, *18* (27), 18022−18035.
(44) Gabai, R.; Ismach, A.; Joselevich, E. Nanofacet Lithography: A New Bottom-Up Approach to Nanopatterning and Nanofabrication by Soft Replication of Spontaneously Faceted Crystal Surfaces. *Adv. Mater.* **2007**, *19* (10), 1325−1330.
(45) Xu, J.; Rechav, K.; Popovitz-Biro, R.; Nevo, I.; Feldman, Y.; Joselevich, E. High-Gain 200 ns Photodetectors From Self-Aligned CdS-CdSe Core-Shell Nanowalls. *Adv. Mater.* **2018**, *30* (20), No. e1800413.
(46) Pan, Z. W.; Dai, Z. R.; Wang, Z. L. Nanobelts of Semiconducting Oxides. *Science* **2001**, *291* (5510), 1947−1949.
(47) Song, X.; Xu, Z.; Gao, B.; Li, X.; Lv, Q.; Zhang, R.; Wang, B.; Zhang, H.; Guo, P.; Ho, J. C. Red-Green-Blue Light Emission From Composition Tunable Semiconductor Micro-Tripods. *Adv. Funct. Mater.* **2024**, *34*, 2403135.
(48) Pan, A.; Zhou, W.; Leong, E. S. P.; Liu, R.; Chin, A. H.; Zou, B.; Ning, C. Z. Continuous Alloy-Composition Spatial Grading and Superbroad Wavelength-Tunable Nanowire Lasers On a Single Chip. *Nano Lett.* **2009**, *9* (2), 784−788.
(49) Shoaib, M.; Wang, X.; Zhang, X.; Zhang, Q.; Pan, A. Controllable Vapor Growth of Large-Area Aligned CdS_xSe_{1-x} Nanowires for Visible Range Integratable Photodetectors. *Nano-Micro Lett.* **2018**, *10* (4), 58.
(50) Li, X.; Tan, Q.; Feng, X.; Wang, Q.; Liu, Y. Wavelength-Controlled Photodetector Based On Single CdSSe Nanobelt. *Nanoscale Res. Lett.* **2018**, *13* (1), 171.
(51) Meng, Y.; Lan, C.; Li, F.; Yip, S.; Wei, R.; Kang, X.; Bu, X.; Dong, R.; Zhang, H.; Ho, J. C. Direct Vapor-Liquid-Solid Synthesis of All-Inorganic Perovskite Nanowires for High-Performance Electronics and Optoelectronics. *ACS Nano* **2019**, *13* (5), 6060−6070.
(52) Rose, A. Performance of photoconductors. *Proc. IRE* **1955**, *43*, 1850−1869.
(53) Bube, R. H. Photoconductivity of the sulfide, selenide, and telluride of zinc or cadmium. *Proc. IRE* **1955**, *43*, 1836−1850.
(54) Zheng, T.; Pan, Y.; Yang, M.; Li, Z.; Zheng, Z.; Li, L.; Sun, Y.; He, Y.; Wang, Q.; Cao, T.; Huo, N.; Chen, Z.; Gao, W.; Xu, H.; Li, J. 2D Free-Standing $GeS_{1-x}Se_x$ with Composition-Tunable Bandgap for Tailored Polarimetric Optoelectronics. *Adv. Mater.* **2024**, *36* (28), No. e2313721.
(55) He, W.; Kong, L.; Yu, P.; Yang, G. Record-High Work-Function P-Type CuBiP2Se6 Atomic Layers for High-Photoresponse Van Der Waals Vertical Heterostructure Phototransistor. *Adv. Mater.* **2023**, *35* (14), 2209995.
(56) Liu, M.; Lagdani, J.; Imrane, H.; Pettiford, C.; Lou, J.; Yoon, S.; Harris, V. G.; Vittoria, C.; Sun, N. X. Self-assembled magnetic nanowire arrays. *Appl. Phys. Lett.* **2007**, *90*, 103105.
(57) Whang, D.; Jin, S.; Wu, Y.; Lieber, C. M. Large-Scale Hierarchical Organization of Nanowire Arrays for Integrated Nanosystems. *Nano Lett.* **2003**, *3*, 1255−1259.

https://doi.org/10.1021/acsami.4c17135
ACS Appl. Mater. Interfaces 2025, 17, 1962−1970